Phys Chem Minerals (2003) 30: 559–569
DOI 10.1007/s00269-003-0350-2

ORIGINAL PAPER

J. E. Amonette · S. M. Heald · C. K. Russell

Imaging the heterogeneity of mineral surface reactivity using Ag(I) and synchrotron X-ray microscopy

Received: 14 November 2002 / Accepted: 1 July 2003

Abstract Microscopic-scale imaging of reduced zones on the surfaces of minerals can be achieved by reaction with dilute Ag(I) solutions and subsequent analysis using synchrotron X-ray microscopy (XRM) above the Ag K-edge (25.5 keV). The principal reductant is Fe(II), but other reductants such as sulfide may contribute. Reduced zones may exist instrinsically, as in the structure of biotite and augite, or may be generated by reaction with chemical agents such as dithionite or treatment with sulfate-reducing bacteria (SRB). We demonstrate the method on flakes of specular hematite and biotite, as well as on thin sections of different rocks (arfvedsonitic granite, oolitic hematite, diabase, and quartz conglomerate) treated with SRB, and discuss possible artifacts that can occur. To our knowledge, this is the only microscopic technique that can image Fe(II) zones on the surface of an Fe-bearing mineral with monolayer sensitivity.

Keywords Silver · XRM · Hematite · Thin sections · Biotite · Sulfate-reducing bacteria · SRB · Granite · Diabase · Conglomerate · Feldspar · Quartz

Introduction

Minerals may serve as large reservoirs of electron-buffering capacity in soils and their surfaces catalyze reactions that may proceed slowly, if at all, in bulk solution. Site-specific assessment of the reactive electron-transfer capacity of minerals, however, presents a formidable challenge that has seemed tractable only recently with the development of new instrumental and theoretical techniques. Appreciation of the significant role played by microorganisms in developing or consuming electron-buffering capacity has further focused interest on the microscopic scale, and led to questions regarding the interactions of classes of microbes such as iron-reducing and sulfate-reducing bacteria with specific minerals. Evident in this process has been the need for imaging techniques that can determine the location of microorganisms on mineral surfaces and the associated impact they have on the reactive electron-buffering capacity of these minerals. Insertion of the green fluorescent protein (gfp) gene plasmid into several species of bacteria (e.g., Neal et al. 2001) has enabled the direct non-lethal identification of living microorganisms on mineral surfaces. Here, we report on a complementary technique that allows imaging of reductive capacity at mineral surfaces on a micron scale.

Our approach is analogous to histological staining techniques in that it requires contact with a stain or dye that irreversibly reacts with the species of interest, remains in place, and can be analyzed by fluorescent or other optical means. The ideal criteria for such a stain include the ability to (1) react with Fe(II) and reduced-S species, as these two elements dominate the reductive capacity associated with minerals, (2) yield a distinct optical signature to avoid artifacts and interferences, and (3) be detected at monolayer concentrations. Further considerations include cost, difficulty of use, and toxicity.

Given the milieu of organic compounds likely to be present on microbially reacted mineral surfaces (among them the gfp), use of a nonvisible portion of the spectrum seems best to avoid interferences. From a detectability standpoint, X-ray fluorescence using a synchrotron excitation source is the method of choice, as it offers superior detection limits and can be employed, using a variety of focusing devices, at the microscopic scale. Such a choice, however, ordains that an oxidizing metal, rather than an organic compound, serve as the stain. Examples of metals commonly used in histological staining include osmium tetroxide (OsO_4), gold chloride ($AuCl_3$), potassium dichromate ($K_2Cr_2O_7$), potassium permanganate ($KMnO_4$), and silver nitrate ($AgNO_3$)

J.E. Amonette (✉) · S.M. Heald · C.K. Russell
Pacific Northwest National Laboratory,
Richland, Washington 99352, USA
e-mail: jim.amonette@pnl.gov
Tel.: +001-509-376-5565
Fax: 001-509-376-3650

(McManus and Mowry 1960; Lillie 1977; Hayat, 1981; Hacker and Gu 2002).

The first of these metals, Os(VIII), is among the most effective metallic oxidants used in tissue staining for electron microscopy because it is highly electron-dense, nonpolar (thus penetrating tissues more effectively than other metals), and can be applied as a vapor. However, it is expensive (ca. \$115 g^{-1}), extremely toxic, and its X-ray properties are unfavorable. The K absorption edge occurs at 73.9 keV, which is too high in energy for typical X-ray microscope optics, and the L_{III} emission line is very near that for the Cu–K_β emission lines which might reasonably be expected in many minerals. For Au(III), similar concerns with regard to expense (ca. \$100 g^{-1}) and unfavorable X-ray properties hold. Here, the K-edge is at 80.7 keV, even higher than that of Os, and the L_{III} emission line is almost identical to that for Zn–K_α emission. Although their K-edge energies are accessible (6–6.5 keV), the Cr(VI) and Mn(VII) oxidants have relatively low X-ray excitation cross sections (ca. 25%). Also, their X-ray emission lines occur in a crowded portion of the spectrum and are soft enough for air absorption to be significant, limiting their ultimate detectability. Moreover, Cr(VI) and Mn(VII) are strong oxidants that would react readily with organic C, and are moderately to strongly toxic. Reduced forms of these metals occur frequently as trace elements in minerals.

Fortunately, Ag(I) (\$8–\$20 g^{-1}) is less expensive than either Os or Au, of comparable toxicity to Au, rare in minerals, and has very favorable X-ray and chemical properties. The K absorption edge is 25.5 keV, within the range that can be handled by current X-ray focusing optics, and the K_α emission lines have no common interferences from elements that would be excited by X-rays just above the Ag–K absorption edge. The high energy of the excitation and emission lines for Ag translate into more efficient excitation (83% fluorescence yield) and transmission than the other metals, and hence a lower detection limit. In terms of chemistry, the reduction potential for the Ag(I)/Ag(0) couple (+ 0.80 V) is just above that for the Fe(III)/Fe(II) couple (+ 0.77 V) making it the mildest oxidant that can be used for imaging of Fe(II). Ag(I) reacts readily with S(-II) to form the Ag_2S minerals argentite and acanthite, both of which are highly insoluble. The stoichiometry of these reactions is also highly favorable with one Ag atom being reduced for each Fe(II) atom oxidized, and two Ag atoms precipitated for each sulfide atom. Despite these strengths and the long-standing use of Ag in histological stains (Murata et al. 1992; Zdolsek et al. 1993; Danscher et al. 1994; Lackie 1996; Hong et al. 2000; Hacker and Gu 2002), some uncertainties remain concerning the use of Ag(I) as the imaging oxidant. These include the degree to which (1) the cationic oxidant reacts with reductive capacity located on positively charged surfaces, (2) the cationic oxidant sorbs to negatively charged sites, thus measuring cation-exchange capacity rather than reductive capacity, and (3) the uncharged metal sticks to the surface and remains where it was reduced.

Some of these issues were examined by Sayin et al. (1979), who used $AgNO_3$ to oxidize Fe(II) in the structure of several K-depleted micas. Silt-sized particles (5–20 μm) of a K-depleted Na-saturated biotite, a phlogopite and a muscovite that were only partly K-depleted, and a lepidolite with little if any K depletion, were reacted with 0.2 N $AgNO_3$ solutions for periods ranging from 1 min to as long as several hours. Examination of the micas with a light microscope after replacing the adsorbed Ag(I) ions with Ba or Mg ions showed no change with the lepidolite and development of an intense blue color in the K-depleted zones of the muscovite and phlogopite. On the basis of circumstantial evidence, the blue color was attributed to Ag(0) colloids, which presumably formed as a result of reduction of Ag(I) adsorbed in the interlayer region by structural Fe(II) in these micas. In the K-depleted biotite, however, no blue color was seen, and significant deposits of metallic Ag formed. These Ag(m) deposits, which took on the order of 6 h to mature and whose nature was confirmed by X-ray diffraction, accumulated on the edges of the biotite flakes when prolonged exposure to the $AgNO_3$ solution was maintained. When the $AgNO_3$ solution bathing the biotite was replaced with deionized H_2O after 1 min of contact, the deposits were more evenly distributed throughout the interlayer region of the biotite. The results of these experiments suggest that the Ag(I) readily exchanges with Na ions on the basal surfaces and interlayer regions of layer silicates and is reduced by structural Fe(II) in a matter of a few hours. Furthermore, the reduced Ag remains in place only when exposure time to the bulk Ag(I) solution is short. Movement and consolidation of Ag(0) atoms into Ag(m) crystals remote from the point of reduction could occur under some circumstances.

Ilton and Veblen (1994a,b) reacted biotites with Ag(I) ions at pH 3 and then mapped the Ag deposited using high-resolution-transmission and scanning-electron microscopies. They noted growths of Ag(0) precipitates at the biotite edges similar to those reported by Sayin et al. (1979) and an inverse correlation of Ag with K content as would be expected from the layer charge decrease coupled to oxidation of structural Fe(II).

To our knowledge, aside from the work of these two groups with micaceous minerals, no reports exist in the literature on the use of Ag(I) to locate and image the zones of reductive capacity on the surfaces of minerals. While one can conceive of direct imaging of Fe(II) on the surfaces of non-Fe-bearing minerals using X-ray microscopy (XRM) coupled with X-ray absorption near-edge structure (XANES) spectroscopy or even Mössbauer spectroscopy, it is currently not possible to separate a small Fe(II) signal from a large Fe(III) background when such Fe(II) occurs on the surface of an Fe-rich mineral such as hematite. In what follows, we provide the first application of this technique to image the reactive zones that result from treatments of a variety of mineral surfaces by both abiotic and biotic reductants.

Experimental

Minerals

Two minerals (a micaceous specular hematite and a ferroan biotite) were treated and analyzed as well as four types of rock (arfvedsonitic granite, oolitic hematite, diabase, and quartz conglomerate). The micaceous specular hematite consisted of small (1–5-mm) flakes derived from a specimen of unknown origin. The ferroan biotite, which was from Faraday township, Ontario, Canada, and obtained from Wards Natural Scientific Establishment (Rochester, NY), also consisted of small flakes and had been studied previously by Scott and Amonette (1988).

The rock samples consisted of (1) an arfvedsonitic granite from Washington Pass, WA, (2) a red oolitic hematite from the Furnaceville Formation, Clinton, NY, (3) a diabase from the Palisade diabase, Jersey City, Hudson County, NJ, and (4) a quartz conglomerate from the Fountain Formation, Fremont County, CO. Literature provided by the supplier (Wards Natural Scientific Establishment, Rochester, NY) indicated that the diabase contained labradorite and colorless augite as the principal minerals and magnetite, ilmenite, and apatite as abundant accessory minerals. Minor amounts of biotite replaced the augite marginally, and chlorite was found in small interstitial patches. Similar literature for the quartz conglomerate indicated that the large pebbles consisted of quartz, quartzite, jasper, and altered potassium feldspar. The sand-sized matrix minerals were quartz and minor unidentified rock fragments. All the rock samples were obtained as unfinished thin sections with mineral surfaces available to react with aqueous solutions. Four thin sections from adjacent cuts on a single specimen were prepared for each rock type, yielding a total of 16 thin sections.

Ag(I) oxidizing solution

On the basis of aqueous solubility and absence of oxidizing or chelating anion, AgF was selected as the form of Ag(I) with which to treat the mineral and rock samples. Because AgF(s) deliquesces, AgF_2(s), which contains Ag(II), was used as the starting compound. The Ag(II) ion oxidizes water in a matter of hours to yield Ag(I), H^+, and O_2. The required amount of the solid was dissolved in water, allowed to react overnight to produce AgF and HF, filtered through a 0.22-μm pore sized filter membrane to remove any solids, and then sparged with N_2 before reaction with mineral surfaces in an anoxic chamber.

Abiotic experiments

Abiotic experiments were conducted with the micaceous specular hematite and ferroan biotite flakes. Reductive capacity beyond that already present in these minerals was generated by treating single flakes with about 2 ml of 0.01 M $Fe(NH_4)_2(SO4)_2$ or a HCO_3-buffered 10 mM $Na_2S_2O_4$ solution for at least 2 h. The mineral flakes were washed 3× with deoxygenated-deionized (DODI) H_2O, reacted with 0.01 M AgF/HF, washed 3× with DODI H_2O, and then dried rapidly under a stream of inert anoxic gas. Specimens that had only contacted DODI H_2O or 0.01 M AgF/HF were also prepared as controls. With the exception of the drying step, all preparation was performed under strictly anoxic conditions. Once the specimens were dry, they were mounted flat on a glass slide using double sticky tape.

Biotic experiments

With the thin-section samples, reductive capacity was generated biotically using the sulfate-reducing bacterium (SRB) *Desulfovibrio desulfuricans* G20 (culture from A.L. Neal and G.G. Geesey, Montana State University). A $4 \times 2 \times 2$ factorial experimental design was applied with three treatment classes (i.e., four rock types, two pHs, and two SRB levels). The pH treatment levels were pH 6.5 and 8.3; those for SRB were SRB present or SRB absent. Thus, each of the four pH/SRB treatment combinations was applied to a unique thin section for a given rock type. All treatments were applied in an anoxic chamber under N_2(g). Prior to treatment, each thin section was rinsed 3× using sterile DODI H_2O. However, no further measure was taken to sterilize the thin sections because of concern about possible artifacts stemming from the sterilization procedure.

The experimental treatments were applied to the thin sections by immersing them for 7 days in a modified lactate C growth medium (Sani et al. 2001) designed for metal toxicity studies. The pH was buffered using bis[tris(hydroxymethyl)methylamino]propane (BTP). At the end of the 7-day incubation period, the thin sections were removed from the growth medium, gently rinsed 3× with sterile DODI H_2O, and then contacted with the Ag(I) oxidizing solution for 10 min. After the Ag(I) treatment, the thin sections were again rinsed 3× with sterile DODI H_2O and allowed to dry in the anoxic chamber. At this point, the samples were considered fixed and were removed from the chamber and stored under ambient conditions until synchrotron XRM analysis could be performed.

The growth medium was analyzed for dissolved H_2S immediately after removal of the thin sections using a methylene-blue based colorimetric procedure available in kit form (Chemetrics, Inc., Calverton, VA). Visual counts of motile SRB in the medium were also made using optical microscopy and a hemacytometer (Hausser Scientific, Horsham, PA).

Synchrotron X-ray microscopy

The XRM analyses were performed at beamline 20ID-B at the Advanced Photon Source, Argonne National Laboratory, Argonne, IL. The micaceous specular hematite and ferroan biotite flakes were analyzed using 25.6 KeV light focused with a glass capillary having a 0.7-μm-diameter exit (Heald et al. 1997, 1999). The specimen was mounted on a movable stage oriented plane-perpendicular to the beam axis. Spot size on the specimen varied with distance from the capillary tip and was adjusted to be approximately equal to one-half of the step size of the scan (typically 2.5–5.0 μm). The nominal spot size, thus, was on the order of 1.25–2.5 μm in diameter. In addition to transmission measurements, a 13-element Ge detector oriented at about 110° to the incident beam axis was used to detect Ag fluorescence produced by the sample.

The thin sections were analyzed in two runs, one starting the day after the initial AgF treatment had been applied to the thin sections, and the other 16 months later. For these analyses, Kirkpatrick–Baez focusing optics were used to achieve either a 3.2-μm^2 (1 day) or 31.9-μm^2 (16 months) spot size taken normal to the beam axis. The specimens were oriented with the plane of the sample approximately 60° from the beam axis, and the 13-element Ge detector was normal to the beam axis (hence, 30° to the plane of the specimen). Spot size on the specimens, thus, was longer in the horizontal dimension than in the vertical dimension by a factor of 1.155, and step size for sample movement in the horizontal direction was corrected by a factor of 0.866 to achieve uniform coverage of the sample. For both runs, the integrated intensities of the K_α emission lines of Ag, Fe, Sr, Rb, and Zr were measured from the detector output using a multichannel analyzer. Iron was selected because Fe(II) is the primary reductant expected in mineral samples. The other three elements were selected because their K absorption edges are between those of Ag and Fe, they are relatively abundant in geological samples, and they might aid in the identification of the mineral phases imaged. Integration times per step ranged from 0.5–15 s and varied inversely with spot size. We note that in all analyses, the position of the 13-element Ge detector relative to the sample was optimized to achieve the maximum total count rate without saturating any of the channels.

Gray-scale images for each element were prepared using ten equally spaced levels of intensity covering the range of intensities for each image. Thus, intensities are not directly comparable across images in an absolute sense.

The detection limit for Ag was estimated for the Kirkpatrick–Baez focusing optics during the first thin-section run by analyzing aqueous solutions of AgF/HF. Solutions containing 0, 0.1, 1, and 10 mM Ag were analyzed in a transmission cell (1.31-mm pathlength) with 20-um-thick Kapton windows. Two separate two-dimensional scans, consisting of 63 data points (i.e., a 3 × 21 array) integrated for 1 s each, were made at each Ag concentration. The average integrated intensity of the Ag–K_α peak, normalized for incident beam intensity, was then calculated for each scan.

X-ray absorption near-edge structure (XANES) spectra were collected at the Ag–K edge for selected points in the images using fluorescence data and for powdered standards (Ag foil and AgCl) using transmission data. After fitting the pre- and postedge regions, the XANES spectra were normalized to constant edge jump to allow comparisons.

Results and discussion

Detection limit for Ag

The normalized Ag-K_α fluorescence signal for the first thin-section run showed a linear response ($r^2 = 0.998$) to the aqueous concentration of Ag from 0–10 mM (Fig. 1). Taking 3× the standard deviation of the signal for the two 0-mM Ag blanks and inserting this value in the regression equation yielded a detection limit of 58 μM. Assuming no divergence in the beam, no scattering by the sample, and accounting for the angle of the specimen with respect to the beam, a volume of about 5.5 pl can be calculated for the portion of the aqueous sample interrogated by the X-ray beam. Further assuming no attenuation of the incident or fluorescent X-rays, the amount of Ag present in this volume at 58 μM concentration would be 34 fg, or about 0.32 fmol. Projecting this result to the surface of a mineral, the detection limit is about 88 amol μm^{-2} for a 1-s integration time. Using the density of Ag(m) (i.e., 10.5 g cm^{-3}), this corresponds to an average thickness of about 0.9 nm (3.1 monolayers of Ag) or a single sphere 184 nm in diameter. Assuming that the detection limit decreases as the square root of the integration time, monolayer detection (or a single 58-nm sphere) could be achieved under these conditions with an integration time of about 10 s.

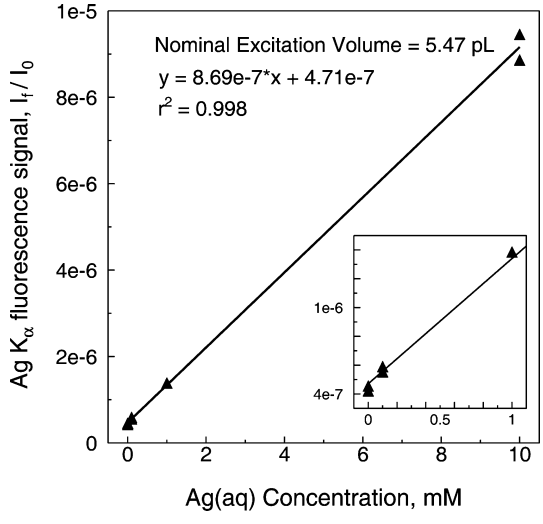

Fig. 1 Ag–K_α fluorescence signals obtained for aqueous Ag solutions using synchrotron X-ray microprobe with 1.8 × 1.8 μm spot size

Abiotic experiments with minerals

When only H_2O was applied, no Ag was seen on either the micaceous specular hematite or the ferroan–biotite flakes. The micaceous specular hematite specimens yielded very little, if any, Ag with the AgF/HF treatment alone, and even with the $Fe(NH_4)_2(SO4)_2$ + AgF/HF treatment. However, significant amounts of Ag were detected on the hematite surfaces for the treatment with $Na_2S_2O_4$ + AgF/HF and yielded patterns suggesting small etch pits or Ag clusters about 5–10 μm in diameter (Fig. 2a).

The ferroan biotite flakes treated with AgF/HF routinely yielded Ag on the surface as would be expected from the Fe(II) content of the mineral and earlier work (Sayin et al. 1979; Ilton and Veblen 1994a,b). Typical images (Fig. 2b) showed narrow contiguous zones of Ag deposition at macrostep edges with occasional high concentrations in broader zones suggestive of etch pits. A linear scan across a macro step edge (indicated by the change in the intensity of the transmitted beam) showed

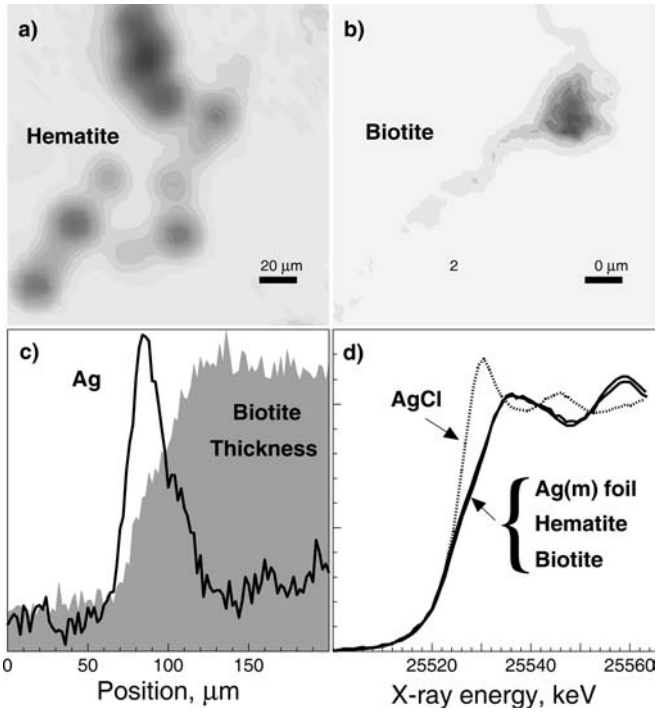

Fig. 2a–d Synchrotron XRM images (170 × 170 μm) of reduced zones (Ag–K_α fluorescence signals) on surfaces of **a** hematite treated with dithionite and then AgF/HF (5-μm step size) and **b** biotite treated with AgF/HF (2.5-μm step size). **c** Lateral scan (200 μm) across edge of biotite treated with dithionite and then AgF/HF showing Ag accumulation in frayed edges (biotite thickness indicated by X-ray absorption values). and **d** Normalized Ag-K-edge XANES spectra taken of reduced zones on hematite and biotite, Ag(m) foil, and AgCl powder

accumulation of Ag almost exclusively at the step edge (Fig 2c). Evidently, the edge sites, which offer access to the interlayer region, were the most reactive. This result is consistent with the similar ionic radii of the K^+ (the main interlayer cation in biotite) and Ag^+ ions and earlier observations (Sayin et al. 1979; Ilton and Veblen 1994a,b). In the absence of macrosteps, large areas of the biotite basal surface yielded no measurable Ag.

XANES spectra collected at the sites of Ag accumulation on the hematite and biotite surfaces were identical to those for Ag(m) and significantly different from that for AgCl (Fig. 2d). All the Ag observed on the mineral surfaces had been reduced. Although it is unclear to what extent photoreduction of adsorbed Ag(I) might have occurred either by visible light or synchrotron X-rays (Calzaferri et al. 2001), a significant, if not dominant, source of electrons remained Fe(II) in the mineral beneath the Ag.

Biotic experiments with rock thin sections

Analyses of the solutions contacting the thin sections treated with SRB yielded substantial amounts ($\geq$ 50 ppm) of dissolved H_2S and high numbers of motile SRB cells ($\geq 2 \times 10^9$ ml^{-1}), indicating the active presence of SRB in the medium and, presumably, on the thin-section surfaces. No motile cells were observed in solutions for the non-SRB-treated thin sections (detection limit of 7.5×10^6 ml^{-1}), although, in the pH-8.3 non-SRB treatment, H_2S levels of 3, 6, 1, and 1 ppm were measured for the granite, oolitic hematite, diabase, and quartz conglomerate, respectively.

A total of 36 separate zones were analyzed on the thin sections that received one of the four treatment combinations (i.e., pH 6.5 + SRB, pH 8.3 + SRB, pH 6.5noSRB, and pH 8.3noSRB). No significant or widespread concentrations of Zr were found in any these zones, nor was any correlation with Ag concentration seen when Zr was present (data not shown). This result is not surprising, given the well-known inertness of Zr minerals and the lack of any redox chemistry associated with Zr(IV) under ambient conditions. We have thus chosen to present images of the Ag, Fe, Rb, and Sr concentrations for five of these zones. In addition to the concentration images, an image of the X-ray density [i.e., $-\log (I/I_0)$] of the thin section is shown, together with correlation plots for Fe, Rb, or Sr with Ag. These eight images and plots are presented as a single plate for each of the five zones in Figs. 3–7. The fluorescent intensity data for the 36 zones analyzed is summarized in Table 1.

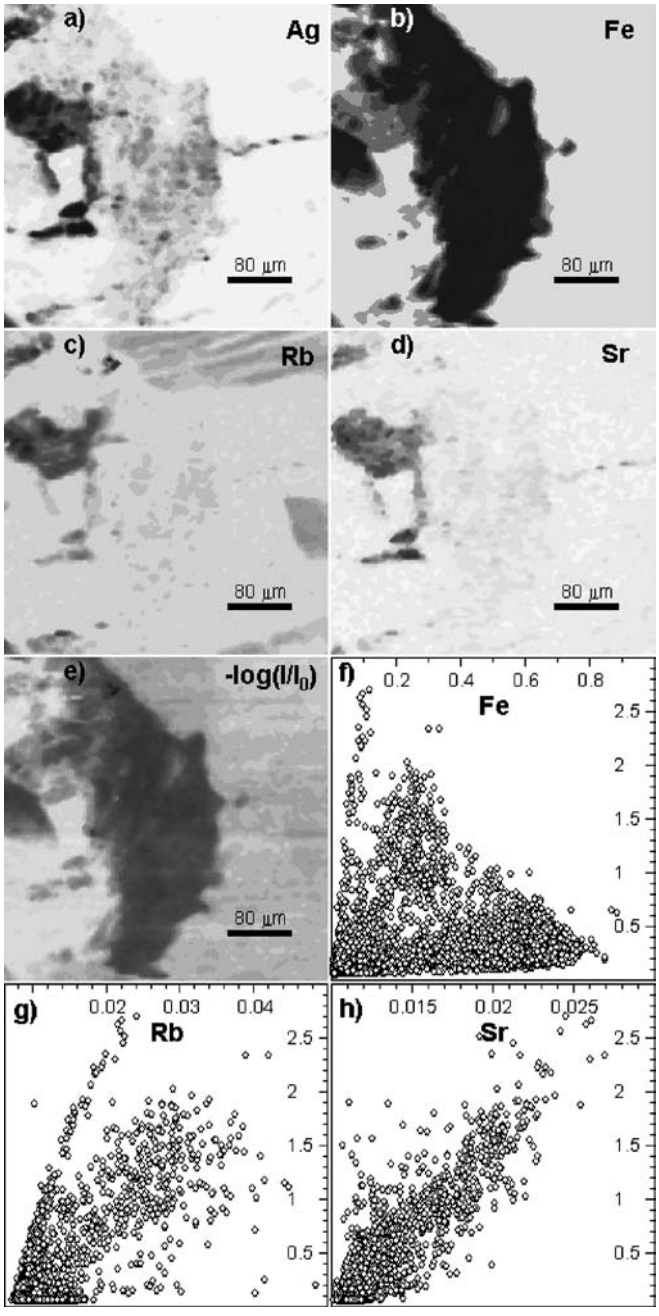

Fig. 3a–h Synchrotron XRM image data for the arfvedsonitic-granite thin section treated with SRB at pH 8.3. Images (400 × 400 μm, 5-μm step size, 1-s integration time) show the relative fluorescent intensities of **a** Ag, **b** Fe, **c** Rb, and **d** Sr, and **e** the X-ray transmission density. *Darker regions* indicate greater intensity. Also shown are correlation plots of the fluorescent intensities obtained for Ag (*y* axis) relative to those for **f** Fe, **g** Rb, and **h** Sr (**x** axis)

Granite

Silver was distributed unevenly on the surface of the arfvedsonitic granite treated with SRB at pH 8.3 (Fig. 3a). The highest concentrations of Ag occurred where high concentrations of Fe, Rb, and Sr (Fig. 3b–d) also occurred. Whereas an apparent strong correlation with Rb and Sr levels was seen, the correlation with Fe was somewhat poorer (Fig. 3f–h). Little or no Ag was seen in the low-Fe regions, but the relative concentrations of Ag in the highest-Fe regions were small compared to those where Fe, Rb, and Sr all occurred

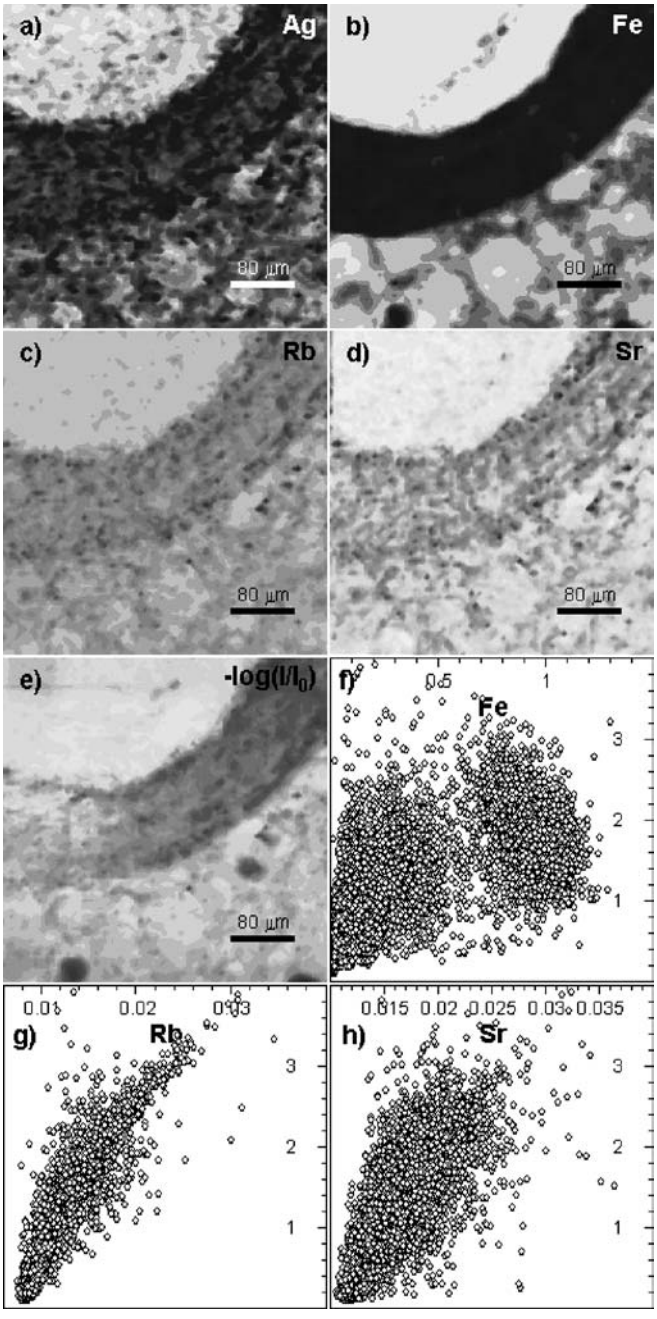

Fig. 4a–h Synchrotron XRM image data for the oolitic–hematite thin section treated with SRB at pH 6.5. Image descriptions as in Fig. 3

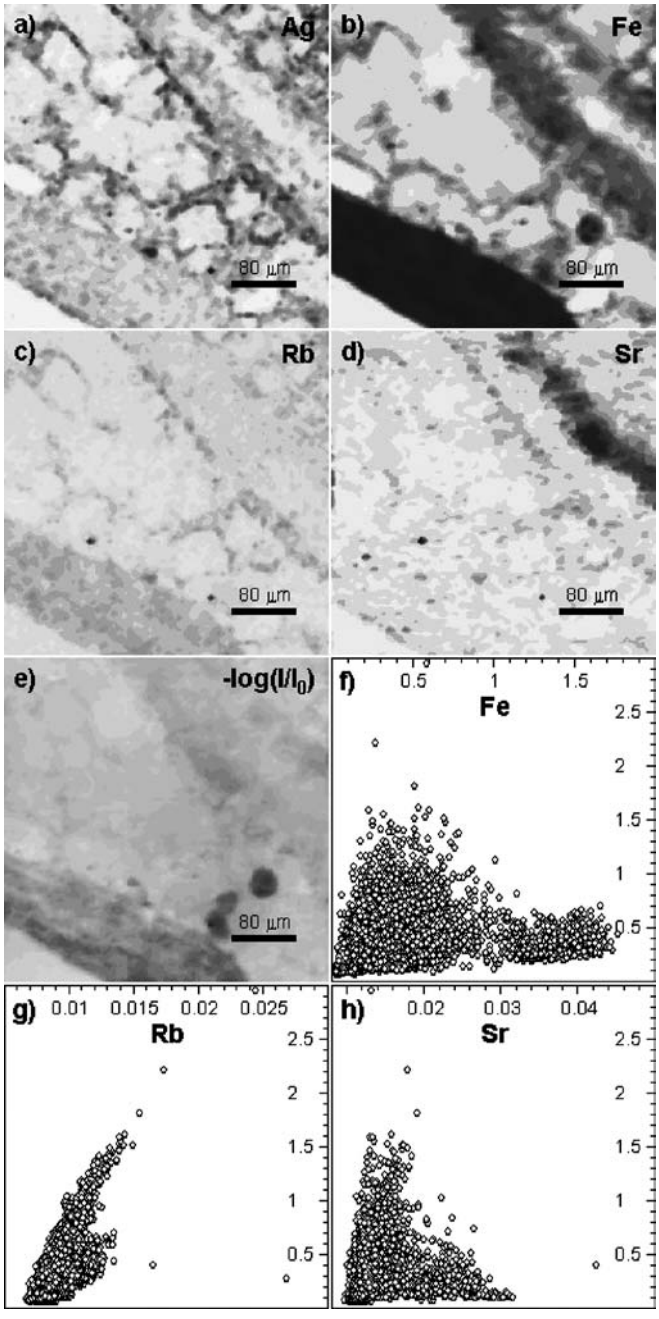

Fig. 5a–h Synchrotron XRM image data for the oolitic-hematite thin section treated at pH 8.3 without SRB present. Image descriptions as in Fig. 3

together. The occurrence of Ag in a linear region in the right central portion of the imaged zone could represent SRB activity located in a surface trench that affords protection to the microorganisms, or a crack in the mineral leading to exposure of the underlying resin used to prepare the thin section.

Correlation plots for Ag with Rb show a curvilinear relationship at the lowest levels of Rb. This relationship is an artifact of secondary fluorescence caused by Ag–K_α X-rays. Absorption of the 25.6-keV synchrotron photon by Ag on the surface yields (with 83% efficiency) a fluorescent K_α X-ray having an energy of 22.1 keV. This X-ray, rather than being collimated like the incident photons, is emitted isotropically and thus excites a larger volume than that irradiated by the synchrotron photons. The net result is artificially high X-ray intensities for elements such as Sr, Rb, and Fe with absorption edges below 22 keV, that are noticeable at the lowest concentrations by the distinctive curvilinear relationship to Ag concentration. Every point in such a curve corresponds to background levels of Sr, Rb, or Fe, but these levels shift to higher measured concentrations as

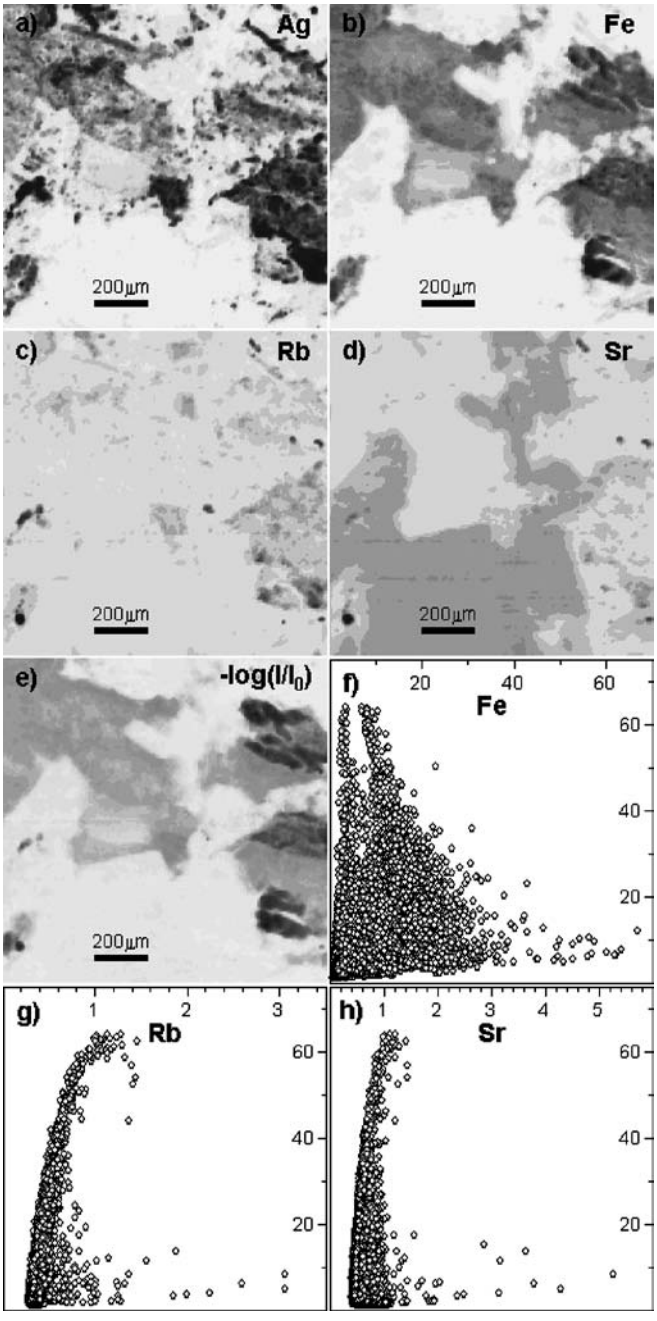

Fig. 6a–h Synchrotron XRM image data for the diabase thin section treated with SRB at pH 8.3. Images are 1200 × 1200 μm, collected sequentially as four separate 400 × 400 μm images with a 10-μm step size and 0.5-s integration time

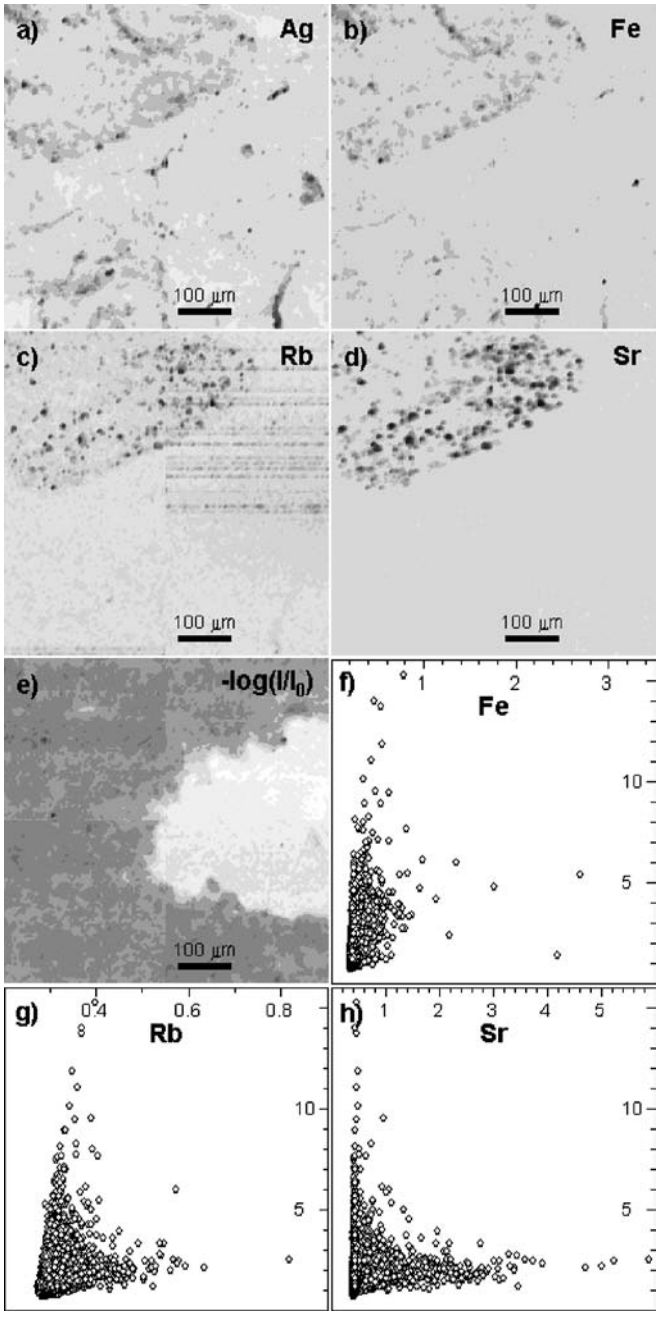

Fig. 7a–h Synchrotron XRM image data for the quartz-conglomerate thin section treated with SRB at pH 6.5. Images are 1200 × 1200 μm, collected sequentially as four separate 400 × 400 μm images with a 10-μm step size, and 0.5-s integration time. Other parameters as in Fig. 3

the Ag concentration increases. Given the very low levels of Sr present in this granite (Table 1), secondary fluorescence dominates, and any perceived correlation with Ag is mostly likely an artifact. Obviously, such artifacts could be avoided by collecting a second scan to map the other elements using synchrotron photons just below the Ag K edge, or by mapping each element individually using photons just above the appropriate absorption edge for that element. These approaches may be impractical given the doubling or quadrupoling of beam time needed. Corrections could be made for the effect, as this is a common problem in conventional X-ray fluorescence spectroscopy, but given the incomplete elemental analysis in the present situation, such corrections would be crude and might introduce even more error into the data. Consequently, all concentration data presented for Fe, Rb, and Sr are uncorrected for secondary fluorescence,

Table 1 Summary of fluorescent intensity data for zones analyzed on rock thin sections

Rock thin section	Bacteria	pH	*n*	Mean fluorescent intensity[a]				Ratio of mean intensities
				Ag[b]	Fe	Rb	Sr	Ag/Fe
Granite (arfvedsonitic)	SRB	8.3	2	310	340	11	5	0.9
Oolitic hematite	SRB	6.5	1	3500	1200	16	18	2.8
	SRB	8.3	1	1100	2200	9	10	0.5
	NoSRB	8.3	1	910	1400	8	10	0.7
Diabase	SRB	6.5	4	810c	1500	27	88	0.5
	SRB	8.3	5	2100d	1800	25	69	1.1
	NoSRB	6.5	5	510c	1000	27	69	0.5
	NoSRB	8.3	6	520c	890	37	71	0.6
Quartz conglomerate	SRB	6.5	5	230e	18	10	29	12.9
	SRB	8.3	2	38f	11	4	10	3.6
	NoSRB	6.5	4	36f	25	4	12	1.4
Treatment combinations	SRB	6.5	10	790g	720	17	52	1.1
	SRB	8.3	10	1200g	1200	17	38	1.0
	NoSRB	6.5	9	300g	570	17	44	0.5
	NoSRB	8.3	7	580g	950	33	62	0.6
Binomial means	SRB	–	20	1000h	970	17	45	1.0
	NoSRB	–	16	420i	740	24	52	0.6
	–	6.5	19	560j	650	17	48	0.9
	–	8.3	17	950j	1100	23	48	0.9
Global means	All		36	740	860	20	48	0.9

[a]Detector counts less the lowest observed count in the image, normalized to I_0 and constant spot size (10 000 um^2)
[b]Treatments within group followed by same letter are not significantly different at $P = 0.05$ level

and must be treated as indicative rather than fully quantitative.

Based on the relative distributions of Fe and Ag it is probable that two types of Fe minerals having different reactivity to Ag were present. The most likely candidates are biotite [$K(Fe^{2+},Mg)_3AlSi_3O_{10}(OH)_2$] and arfvedsonite [$Na_3Fe^{2+}{}_4Fe^{3+}Si_8O_{22}(OH)_2$]. Based on (1) our analyses of biotite flakes (Fig. 2), which showed little reactivity on the basal surfaces, (2) the expected relative reactivities of arfvedsonite and biotite from the Bowen reaction series, and (3) calculated estimates of minimum reduction potentials for Fe in ferrosilite (+ 0.59 V) and annite (+ 0.71 V) (Amonette 2003), it seems likely that the regions with the highest Ag concentrations are associated with the arfvedsonite, whereas those with the highest Fe concentrations are associated with biotite. This assignment suggests that most of the Rb present in the reactive phase is substituted for Na in the arfvedsonite, probably in the M4 or A sites described by Klein and Hurlbut (1977, p. 411).

Hematite

The oolitic hematite treated with SRB at pH 6.5 yielded the highest average Ag concentration of all the zones tested and a strong association of Ag with Fe was seen (Fig. 4a,b). The Fe was distributed primarily as 100-μm-thick hematite coatings on large quartz sand grains, with lesser amounts cementing very fine sand and silt grains located in the interstices between the larger sand particles. Although the correlation between Ag and Fe is evident, also evident is the presence of Ag on the quartz grains themselves, suggesting the presence of SRB colonies on the entire rock surface. A preference for Fe is seen, but it is not exclusive. A small Fe-rich nodule, about 40 μm in diameter at the lower left margin of the image, evidently was not reactive to Ag, however, and may represent a different form of Fe such as magnetite (Fe_3O_4). The apparent correlations of Ag with Rb and Sr (Fig. 4g,h) are severely distorted by secondary fluorescence effects.

In contrast, oolitic hematite sections treated at pH 8.3 with SRB yielded about 32% as much Ag as the pH 6.5 treatments (image not shown, Table 1). Treatment at pH 8.3 in the absence of SRB, however, still yielded about 25% as much Ag as the pH 6.5 treatments (Table 1). A much poorer correlation with the primary hematitic Fe was seen in this sample, with most of the Ag locating at the margins of interstitial sand grains (Fig. 5a,b). It is likely that this Ag is adsorbed to clay minerals such as illite, although the possibilities of adventitious microbial activity or exposed resin cannot be excluded. Secondary fluorescence dominates the Rb:Ag relationship (Fig. 5g), but clear evidence of an Sr zone with little Ag association is seen (Fig. 5d).

Diabase

The diabase thin sections had the most complicated mineralogy, and yielded correspondingly complex Ag distribution patterns. For the diabase treated with SRB at pH 8.3, Ag distribution was largely correlated with that of Fe (Fig. 6a,b) although a few regions with high Ag concentrations, notably at the upper margin and

central left margin of the image, had little or no Fe associated with them. In general, little Ag was deposited on the labradorite, which represented about half the total surface and is mapped as the moderately high-Sr region (Fig. 6d). The distributions of Rb and Sr were strongly influenced by secondary fluorescence (Fig. 6g,h) and showed little correlation with that of Ag.

Several Fe-bearing minerals (magnetite, ilmenite, olivine, augite, and biotite) are most likely present, and some guesses as to their identity can be made from the relative Fe concentrations, X-ray densities, and reactivity towards Ag shown in the images (Fig. 6a,b,e). The X-ray densities of these minerals (mol electrons cm^{-3}) decrease as magnetite > ilmenite > olivine > augite > biotite, and their Fe densities decrease as magnetite $\gg$ ilmenite $\approx$ augite > olivine $\approx$ biotite, where clinoferrosilite, fayalite, and annite are used to represent augite, olivine, and biotite. Starting with the X-ray densities (Fig. 6e), the three dense regions on the right margin are most likely magnetite or ilmenite. Based on their reactivity towards Ag, we suggest that the top and bottom of these are magnetite (low reactivity) whereas the middle is ilmenite. The identity of the small high-Ag region located in the center of the image is probably olivine, whereas the low-Ag region just to the left may be biotite. The remainder of the Fe-rich region is most likely augite, which seems to have a moderate activity towards Ag.

Diabase treated at pH 8.3 without SRB present yielded similarly complex images (images not shown), but total Ag levels were about 25% of those for the SRB-treated sections (Table 1). Some of this decrease no doubt was due to the Fe levels being only about 50% of those seen in the SRB-treated sections(Table 1). At pH 6.5, little effect of SRB treatment was seen (images not shown, Table 1).

Quartz conglomerate

Of the four rocks examined, the quartz conglomerate had the lowest Fe content (Table 1). Not surprisingly, then, the Ag levels were much lower than for the other thin sections. In the specimen treated at pH 6.5 with SRB, the Ag was distributed semirandomly across the surface, with some apparent concentration at grain boundaries and cracks (Fig. 7a). The Fe, Rb, and Sr distributions were largely concentrated on one grain in the upper left portion of the image, and exhibited only slight correlation with Ag (Fig. 7b–d; f–h). At pH 8.3, or in the absence of SRB, the Ag levels were only about 15% of those seen at pH 6.5 with SRB (Table 1).

A photograph of the pH-6.5 SRB-treated surface taken at the time of XRM analysis shows many shiny spheroidal deposits on the surface, some of them as large as 100 μm across (Fig. 8a). They seem associated with a particular grayish colored region, the margins of which are blackened. From the X-ray density image

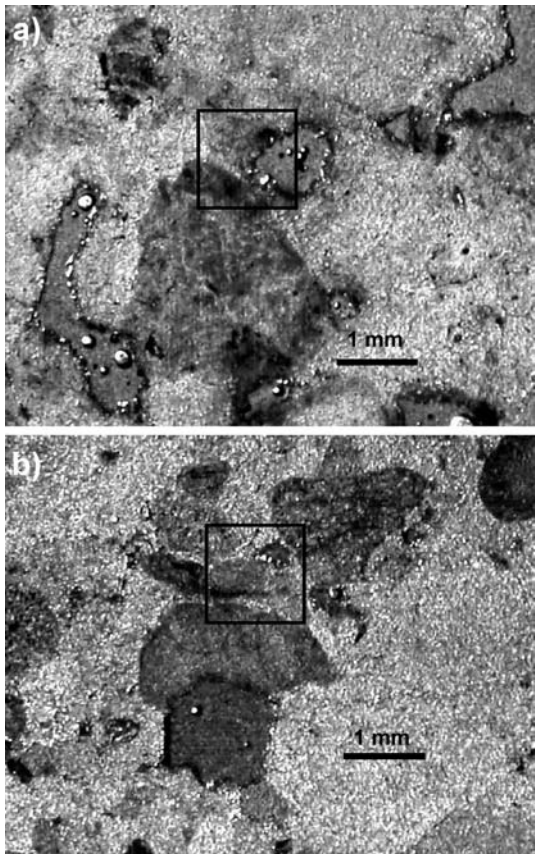

Fig. 8a–b Reflected light images of surface of quartz-conglomerate thin section treated at pH 6.5 with **a** SRB present, and **b** SRB absent. *Black rectangles* indicate regions analyzed by synchrotron XRM

(Fig. 7e), which shows a large low-density zone where the gray area occurs in Fig. 8a, and from a visual inspection of the surface, it is likely that the gray regions correspond to zones where the original rock is no longer present and the underlying resin is exposed. Other large blackened areas also can be seen on some of the other minerals present. A comparison with the pH-6.5 surface that was not treated with SRB (Fig. 8b) shows only a few spheroidal deposits and very few blackened areas. The large deposits most likely consist of Ag(m) derived by reaction with the resin and subsequently accumulated into larger particles as a result of an inability to wet the resin surface. The black areas in the SRB-treated thin section (Fig. 8a) most likely are deposits of Ag sulfide and represent areas of active SRB colonization at the time of Ag treatment. None of the other rock types analyzed showed deposits of either type (shiny or black), even though the Ag contents measured by XRM were substantially larger. Indeed, efforts to image the spheroidal deposits by XRM were unsuccessful. We suspect that the intensity of the incident beam caused the deposits to disintegrate and leave the surface. For this type of surface (exposed resin), then, it seems that the Ag deposits are mobile and thus do not map the reductive capacity of the surface reliably.

Statistical Analyses

The average Ag concentrations from each of the thirty-six zones analyzed were weakly ($r = 0.34$, $P = 0.04$) correlated with the presence of SRB. A highly significant ($r = 0.75$, $P = 1.1\text{e-}7$) correlation, however, was achieved between average Ag and average Fe concentrations. All other possible correlations of Ag (i.e., with pH, Rb, or Sr) were nonsignificant ($P > 0.05$).

One-way completely randomized analyses of variance (ANOVA) were performed for the measured Ag concentrations obtained for (1) treatment combinations (i.e., pH and SRB) with the diabase and quartz-conglomerate zones separately, (2) pH and SRB treatment combinations with all 36 zones taken together, and (3) each treatment class (i.e., pH or SRB) with all zones. Not enough replicates were taken to allow ANOVAs to be run on the granite and oolitic–hematite datasets. Of these ANOVAs, only three showed significant differences at the $P \leq 0.05$ level among the possible treatments (Table 1). For the diabase, the pH-8.3 SRB treatment yielded significantly higher Ag levels than the other three treatments. For the quartz conglomerate, the pH-6.5 SRB treatment yielded significantly higher Ag levels than the pH-8.3 SRB and pH-6.5 non-SRB treatments (this result, however, may reflect differences in the amount of resin exposed rather than an SRB-treatment effect). For the entire set of 36 zones analyzed, the zones treated with SRB had significantly higher levels of Ag than the zones that were not treated with SRB. Removal of the quartz-conglomerate data from the last ANOVA still resulted in significantly higher levels of Ag in the SRB-treated samples.

A casual examination of the mean fluorescent intensity data (Table 1) show a high degree of variability in the Fe data for a given rock type. To attempt to eliminate some of this variability, the mean Ag data were normalized for mean Fe content on the assumption that Fe was the primary reductant. These data (Table 1) clearly show the impact of SRB treatments and pH on Ag accumulations and yielded the same ANOVA results.

With regards to pH, it is interesting that the oolitic hematite and quartz conglomerate behave similarly, with higher Ag accumulations at pH 6.5 than at pH 8.3, whereas the opposite trend with pH is observed for the diabase samples (Fig. 9). These seemingly disparate results may stem from the different Fe mineralogy present in these samples. The Fe in the quartz-conglomerate and oolitic-hematite samples is primarily, if not exclusively, in an oxide form, and would be more soluble at pH 6.5 than at pH 8.3. In the diabase, on the other hand, the Fe is dominantly found in silicate minerals, which would tend to be more soluble at pH 8.3 than at pH 6.5. From the standpoint of establishing maximum reductive capacity in a subsurface zone by stimulating SRB or other reductive bacteria, then, knowledge of the Fe mineralogy could dictate the appropriate pH level at which to operate.

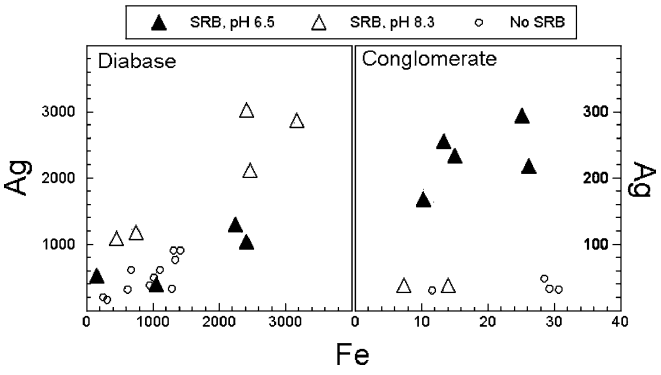

Fig. 9a–b Correlation plots of the mean fluorescent intensity data for Ag and Fe collected for **a** 20 images of diabase thin sections, and **b** 11 images of quartz–conglomerate thin sections treated either pH 6.5 of 8.3 in the presence or absence of SRB

Conclusions

The use of the Ag(I)/Ag(0) couple to image reactive zones on mineral surfaces shows great promise. A wide range in reactivity is seen and near monolayer sensitivity can be obtained using the synchrotron X-ray microscope. In general, the amount of Ag observed on the surface is correlated with the Fe content of the minerals beneath, notable exceptions being magnetite, which does not appear to react with Ag(I), and exposed resin, which does react. Abiotically generated reductive zones can be imaged on specular hematite, as can reactive edges on biotite flakes. Towards the goal of imaging bacterially stimulated reductive zones, the extent to which the HF in the AgF/HF treatment biases the treatment towards a measurement of HF solubility of Fe(II) rather than bacterially reduced Fe(II) and sulfide is unclear. There is no doubt that an effect of SRB on measurable Ag content exists, however, and that in some instances this effect may depend more on the physical properties of the surface (e.g., cracks, fissures, and scratches) than on the Fe content of the mineral to which the bacteria are attached.

Several uncertainties exist in the method. First among these are the role of nonreducing cation-exchange sites and light on the Ag results obtained. It may be that a two-step process needs to be developed, in which Ag(I) ions react with the mineral surfaces in the dark, and then the remaining sorbed Ag(I) ions are removed from the surfaces by cation exchange with a divalent cation such as Mg or Ba. The HF effect can ostensibly be eliminated by adding a stoichiometric amount of silica to the AgF/HF solution to neutralize the HF. Although the reactivity of Ag with the resin used to prepare the thin section is expected to be lower than other potential oxidants, it is still substantial, and can lead to artifacts in the data. Loosely cemented rocks, such as the quartz conglomerate used in this study, soils, and sediments, will not yield intact resin-free surfaces. This problem might eventually be solved by the development and use of resin-specific coatings that block reaction with Ag(I) while leaving the mineral surface in its original state.

Acknowledgements We thank Dale Brewe for assistance with the focusing-capillary X-ray microscope and Kevin M. Rosso for assistance in collecting the abiotic mineral data. This manuscript benefited from helpful reviews by Klaus Pecher and Eugene Ilton. This research was supported in part by the Natural and Accelerated Bioremediation Research (NABIR) Program, Office of Biological and Environmental Research (OBER), US Department of Energy (DOE) and in part by the Laboratory Directed Research and Development program at the Pacific Northwest National Laboratory (PNNL). The PNNL is operated for DOE by Battelle Memorial Institute under contract DE-AC06–76RL0 1830.

References

Amonette JE (2003) Iron redox chemistry of clays and oxides: environmental applications. In: Fitch A (ed.) Electrochemistry of clays. CMS Workshop Lectures Vol 10. Clay Minerals Society, Aurora, CO, pp 89–146

Calzaferri G, Bruhwiler D, Glaus S, Schurch D, Currao A, Leiggener C (2001) Quantum-sized silver, silver chloride and silver sulfide clusters. J Imaging Sci Technol 45: 331–339

Danscher G, Stoltenberg M, Juhl S (1994) How to detect gold, silver and mercury in human brain and other tissues by autometallographic silver amplification. Neuropathol Appl Neurobiol 20: 454–467

Greffie C, Benedetti MF, Parron C, Amouric M (1996) Gold and iron oxide associations under supergene conditions: an experimental approach. Geochim Cosmochim Acta 60: 1531–1542

Hacker GW, Gu J (2002) Gold and silver staining: techniques in molecular morphology. CRC Press, Boca Raton, FL

Hayat MA (1981) Fixation for electron microscopy. Academic Press, New York

Heald SM, Brewe DL, Barg B, Kim KH, Brown FC, Stern EA (1997) Micro-XAS using tapered capillary concentrating optics. J Physique IV 7(C2): 297–301

Heald SM, Brewe DL, Stern EA, Kim KH, Brown FC, Jiang DT, Crozier ED, Gordon RA (1999) XAFS and micro-XAFS at the PNC-CAT beamline. J Synchrotron Rad 6: 347–349

Hong LJ, Mubarak WAE, Sunami Y, Murakami S, Fuyama Y, Ohtsuka A, Murakami T (2000) Enhanced visualization of weak colloidal iron signals with Bodian's protein silver for demonstration of perineuronal nets of proteoglycans in the central nervous system. Arch Histol Cytol 63: 459–465

Ilton, ES, Veblen, DR (1994a) Interaction of metal-bearing solutions with micas: Electron microscopy and XPS of experimental and natural samples. EOS Trans. American Geophysical Union, Spring Meeting Suppl. 75: 190

Ilton, ES, Veblen, DR (1994b) Coupled sorption/reduction of silver and other multivalent metals by ferrous micas: insights from electron microscopy and XPS. In Andren AW, Bober TW (eds) Argentum 1994: Proceedings 2nd International Conference Transport, Fate, and Effects of Silver in the Environment. University of Wisconsin Sea Grant Institute, Madison, WI

Klein C, Hurlbut CS (1977) Manual of mineralogy (after James D. Dana), 20th ed. Wiley, New York

Lackie PM (1996) Immunogold silver staining for light microscopy. Histochem Cell Biol 106: 9–17

Lillie RD (1977) H. J. Conn's biological stains, 9th ed. Williams and Wilkins Company, Baltimore

McManus JFA, Mowry RW (1960) Staining methods histologic and histochemical. Paul B. Hoeber Inc., New York

Murata F, Tsuyama S, Ihida K, Kashio N, Kawano M, Li ZZ (1992) Sulfated glycoconjugates demonstrated in combination with high iron diamine thiocarbohydrazide-silver proteinate and silver acetate physical development. J Electron Microsc 41: 14–20

Neal AL, Techkarnjanaruk S, Dohnalkova A, McCready D, Peyton BM, Geesey GG (2001) Iron sulfides and sulfur species produced at hematite surfaces in the presence of sulfate-reducing bacteria. Geochim Cosmochim Acta 65: 223–235

Sani RK, Geesey GG, Peyton BM (2001) Assessment of lead toxicity to Desulfovibrio desulfuricans G20: influence of components of lactate C medium. Adv Environ Res 5: 269–276

Sayin M, Beyme B, von Reichenbach H (1979) Formation of metallic silver as related to iron oxidation in K-depleted micas. Dev Sedimentol 27: 177–186

Scott AD, Amonette JE (1988) Role of iron in mica weathering. In: Stucki JW, Goodman BA, Schwertmann U (eds) Iron in soils and clay minerals. D Reidel, Dordrecht, pp 537–623

Zdolsek JM, Roberg K, Brunk UT (1993) Visualization of iron in cultured macrophages — a cytochemical light and electron-microscopic study using autometallography. Free Radical Biol Med 15: 1–11